JACS
JOURNAL OF THE AMERICAN CHEMICAL SOCIETY
Article
pubs.acs.org/JACS

Nanoporous Metal Oxides with Tunable and Nanocrystalline Frameworks via Conversion of Metal–Organic Frameworks

Tae Kyung Kim,[†,§] Kyung Joo Lee,[†,§] Jae Yeong Cheon,[‡] Jae Hwa Lee,[†] Sang Hoon Joo,*[,‡] and Hoi Ri Moon*[,†]

[†]Interdisciplinary School of Green Energy and [‡]School of Nano-Bioscience and Chemical Engineering, KIER-UNIST Advanced Center for Energy, and Low-Dimensional Carbon Materials Center, Ulsan National Institute of Science and Technology (UNIST), UNIST-gil 50, Ulsan 689-798, Republic of Korea

Supporting Information

ABSTRACT: Nanoporous metal oxide materials are ubiquitous in the material sciences because of their numerous potential applications in various areas, including adsorption, catalysis, energy conversion and storage, optoelectronics, and drug delivery. While synthetic strategies for the preparation of siliceous nanoporous materials are well-established, nonsiliceous metal oxide-based nanoporous materials still present challenges. Herein, we report a novel synthetic strategy that exploits a metal–organic framework (MOF)-driven, self-templated route toward nanoporous metal oxides via thermolysis under inert atmosphere. In this approach, an aliphatic ligand-based MOF is thermally converted to nanoporous metal oxides with highly nanocrystalline frameworks, in which aliphatic ligands act as the self-templates that are afterward evaporated to generate nanopores. We demonstrate this concept with hierarchically nanoporous magnesia (MgO) and ceria (CeO_2), which have potential applicability for adsorption, catalysis, and energy storage. The pore size of these nanoporous metal oxides can be readily tuned by simple control of experimental parameters. Significantly, nanoporous MgO exhibits exceptional CO_2 adsorption capacity (9.2 wt %) under conditions mimicking flue gas. This MOF-driven strategy can be expanded to other nanoporous monometallic and multimetallic oxides with a multitude of potential applications.

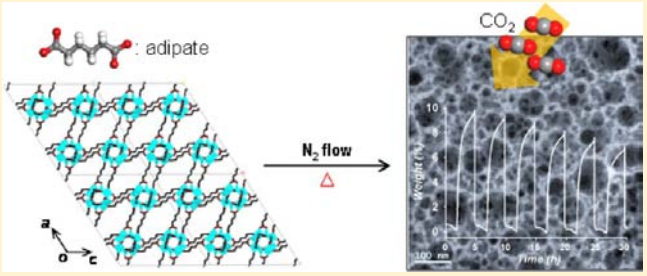

1. INTRODUCTION

Nanoporous metal oxide materials have been of pivotal importance in the material sciences, and their promise has been widely demonstrated in various areas, including adsorption, catalysis, energy conversion and storage, optoelectronics, and biological platforms.[1] Synthetic strategies for the preparation of nanoporous silicas are well-established. Soft-templating routes that rely on the synergistic self-assembly of surfactant and silicate species, followed by calcination, generate mesoporous silica materials with tunable mesostructure and pore size.[2−4] In contrast, the application of a similar synthetic principle to nonsiliceous compositions has rarely been successful thus far, making the preparation of nonsiliceous nanoporous materials challenging.[5,6] This difficulty predominantly stems from the uncontrollable hydrolysis and condensation of nonsiliceous metal oxide precursors and the breakdown of the surfactant-metal oxide composite structure upon calcination. Even though nanoporous structures are formed via surfactant-assisted, soft-templating routes, the resulting materials are commonly composed of amorphous or semicrystalline frameworks, rather than the nanocrystalline state which is more desirable for various applications.[7] In order to circumvent these problems, new synthetic approaches to nanoporous nonsiliceous metal oxides have been developed, including evaporation-induced self-assembly,[8,9] nanocasting,[5,6,10] nanoparticle self-assembly,[11,12] and reinforced crystallization.[7,13]

Herein, we report a novel synthetic method that exploits the thermal conversion of metal–organic frameworks (MOFs) into hierarchically nanoporous metal oxides with nanocrystalline frameworks without using structure-directing surfactants. MOFs are well-ordered crystalline solids, which are mostly composed of metal–oxygen coordinating clusters as secondary building units (SBUs) and aromatic organic linkers.[14,15] Large surface areas and porosities as well as a high degree of tunability for both the organic and inorganic building blocks of their structures enable the potential use of MOFs in a wide range of applications, including gas storage and separation, membranes, catalysis, sensing, and biomedical imaging.[16−21] Recently, a new, burgeoning direction in the field of MOFs has been their use as 'precursors' of new nanostructured materials, primarily via thermolysis.[22−35] During the thermal decomposition process, the metal ions in the MOFs can be transformed into metallic or metal oxide nanoparticles, and the organic ligands can be converted into carbonaceous structures. This MOF-driven method has been successful for preparing nanoporous carbons with controlled surface areas and porosities.[22−27] By

Received: February 23, 2013
Published: May 7, 2013

   dx.doi.org/10.1021/ja401869h | J. Am. Chem. Soc. 2013, 135, 8940−8946

contrast, the preparation of nanoporous metal oxides from MOFs has not yet been successful; instead, nonporous metal oxide nanoparticulates have been generated, presumably due to the secondary agglomeration of the metal oxide nanocrystals (NCs) during the thermolysis of the MOFs.[28−33]

The key to our approach toward hierarchically nanoporous metal oxide materials with nanocrystalline frameworks lies in the use of MOFs based on aliphatic carboxylate ligands, which are thermally less stable and much more labile, even under inert atmosphere, than aromatic ligands. During the thermolysis of a crystalline, *aliphatic* carboxylate ligand-based MOF (*aph*-MOF), the ligands were transformed into organic (or carbogenic) moieties via chemical decomposition and were confined as vesicles in the solids. The organic vesicles acted as self-generated porogens, which later were converted into nanopores; they also prevented aggregation of the metal oxide nanocrystals. Finally, upon thermolysis at higher temperature, the confined organic moieties evaporated, generating highly porous nanostructures comprising nanocrystalline metal oxides (Scheme 1). We note that the control

Scheme 1. Schematic View of the Direct Conversion from *aph*-MOF to *np*-Metal Oxide by Heating under Nitrogen Atmosphere

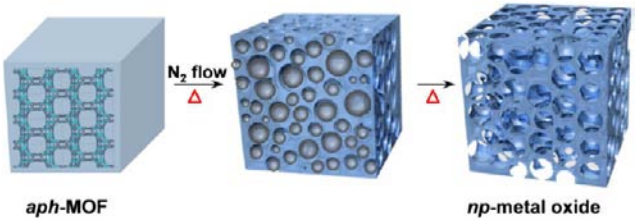

of the retention time and the evaporation rate of the organic moieties in the host solid were critical for the successful formation of nanoporous metal oxides with nanocrystalline frameworks. We demonstrate our MOF-driven approach to nanoporous metal oxides with the successful preparation of nanoporous MgO and CeO_2 with nanocrystalline frameworks. The pore sizes of these nanoporous materials could be readily tuned by simple control of experimental factors. Furthermore, we demonstrate that nanoporous MgO materials exhibit exceptionally high CO_2 absorption capacity with recyclability. Our MOF-driven method is simple yet powerful to generate nanoporous metal oxide structures. We believe that the applicability of our method to other nanoporous metal oxides as well as metals is highly viable because MOFs can be prepared with enormous structural and compositional diversities.

2. RESULTS AND DISCUSSION

For the preparation of an *aph*-MOF, commercially available, inexpensive adipic acid ($HOOC(CH_2)_4COOH$) was chosen as the aliphatic ligand. The solvothermal reaction of Mg-$(NO_3)_2{\cdot}6H_2O$ and adipic acid in a mixture of *N*,*N*−dimethylacetamide (DMA) and methanol (MeOH) yielded colorless block-shaped crystals of $[Mg_4(adipate)_4(DMA)(H_2O)]{\cdot}5DMA{\cdot}2MeOH{\cdot}4H_2O$ (Mg-*aph*-MOF). Single crystal X-ray diffraction data revealed that the structure of Mg-*aph*-MOF was constructed of Mg−O chains and adipates as the bridging ligands (Figure 1). The Mg-*aph*-MOF contained four crystallographically independent magnesium atoms in distorted octahedral coordination geometries. Of the four Mg atoms, two

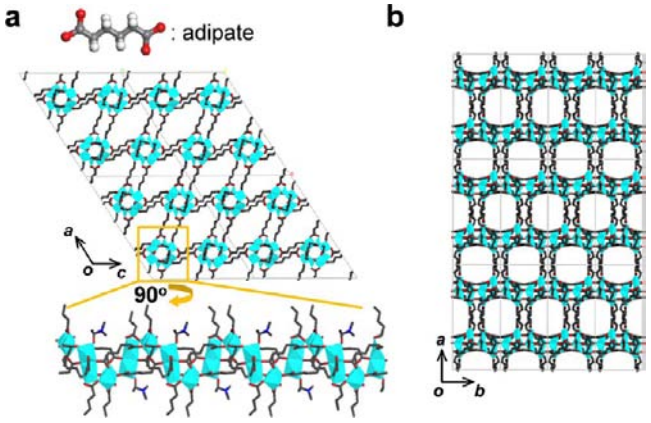

Figure 1. Single-crystal X-ray structure of Mg-*aph*-MOF. (a) 3D framework formed by association of secondary building units (SBUs) of Mg−O chain and organic ligands, adipate. The yellow rectangle indicates the (SBU) of the Mg−O chain. (b) Structure projected along the *c*-axis, showing 11 × 11 Å channels. Hydrogen atoms and guest molecules are omitted for clarity. Color scheme: C, gray; O, red; and Mg, light blue.

Mg^{2+} ions were coordinated by five oxygen atoms, among which four were provided by the adipate ligands and one was donated by a solvent molecule, such as DMA or water. The other two Mg^{2+} ions were coordinated with six oxygen atoms of the adipate ligands (see Figure S1). The infinite metal−ligand coordinations generated 1D Mg−O chains as SBUs, which were bridged with four neighboring chains by adipate ligands in four different directions to construct 11 × 11 Å 3D pores containing guest solvent molecules, DMA, MeOH, and water. In the thermogravimetric analysis (TGA) trace of the as-synthesized Mg-*aph*-MOF (see Figure S2), the guest solvent molecules that occupied the void spaces of Mg-*aph*-MOF were removed during heating from room temperature to ∼220 °C. To liberate the coordinated DMA and water molecules from Mg^{2+}, the temperature required was 320 °C, and decomposition of Mg-*aph*-MOF ensued above ∼330 °C.

Based on the TGA results, the decomposition of Mg-*aph*-MOF was performed at 500 °C by heating with a ramping rate of 5 °C/min under a nitrogen flow of 60 cc/min (Figure 2). After maintaining the temperature at 500 °C for 12 h, the colorless crystalline Mg-*aph*-MOF was converted into an off-white solid, which was identified as single-phase cubic magnesium oxide by X- ray powder diffraction (XRPD) patterns, coincident with JCPDS file no. 89-7746 (Figure 2a). Calculation of the crystalline size of MgO, estimated by applying the Debye−Scherrer equation to the (200) reflection, indicated the formation of MgO nanocrystals of 6.3 nm in diameter. Surprisingly, the transmission electron microscopy (TEM) images of the resultant solid (Figure 2c,d) showed that these MgO nanocrystals comprised highly nanoporous structures (*np*-MgO-500). The *np*-MgO-500 had hierarchical pore structures, wherein both mesopores (a few tens of nanometers) and macropores (50−100 nm) existed. The clear lattice fringes in the high-resolution TEM image (Figure 2d) of *np*-MgO-500 as well as the corresponding selected area electron diffraction image (Figure 2d, inset) also indicated that the nanoporous solids were constructed from MgO NCs. The MgO NCs, which were interconnected in the nanoporous solid (*np*-MgO-500) wall, did not undergo larger secondary agglomeration and coexisted with a small amount of carbon

dx.doi.org/10.1021/ja401869h | J. Am. Chem. Soc. 2013, 135, 8940−8946

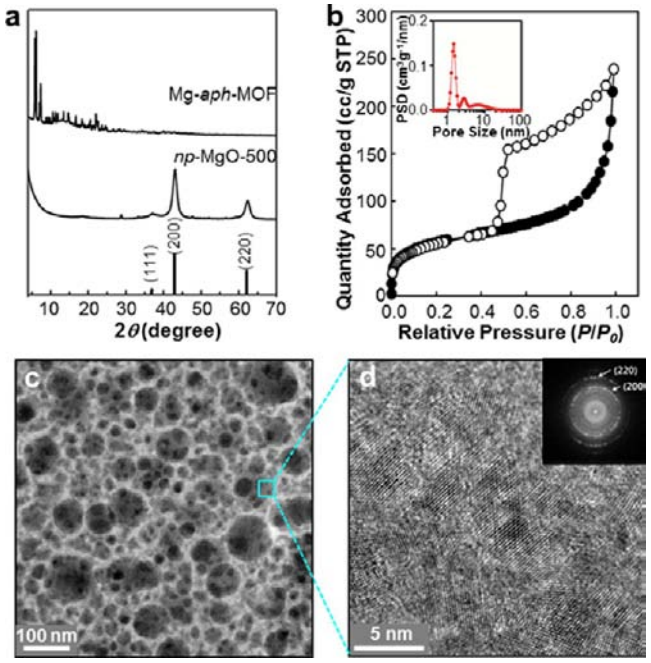

Figure 2. Characterization of *np*-MgO-500. (a) Comparison of XRPD patterns of Mg-*aph*-MOF (top) and *np*-MgO-500 (bottom). (b) N_2 sorption isotherm and NLDFT pore size distribution curve (inset) of *np*-MgO-500. (c) Dark-field TEM image of *np*-MgO-500. (d) HR-TEM image of framework walls in *np*-MgO-500.

(1.79 wt %). In order to assess the porous structure of the *np*-MgO-500, a nitrogen adsorption−desorption measurement was conducted. As shown in Figure 2b, the *np*-MgO-500 showed a typical type IV isotherm with an H2 type hysteresis loop over a relative pressure range of $0.5 < P/P_0 < 0.95$, characteristic of cage-like pore structures with large mesopores and narrow channel interconnections. The pore size distribution curve of *np*-MgO-500 analyzed by the nonlocal density functional theory (NLDFT) algorithm (Figure 2b, inset) exhibited micropores centered at 1.4 nm as well as mesopores around 2.7 nm and a broad distribution from 4 to 20 nm. Hence, the *np*-MgO-500 was composed of triply hierarchical porous structures of micro-, meso-, and macropores. The Brunauer−Emmett−Teller (BET) surface area for the *np*-MgO-500 was 200 m^2/g, and the total pore volume was 0.37 cc/g. Remarkably, a significant portion of the total pore volume was contributed by micropores, with their value reaching 0.13 cc/g. This synthetic method was successfully extended to the preparation of nanoporous CeO_2 (*np*-CeO_2) from Ce-*aph*-MOF ($Ce_2(adipate)_3{\cdot}2DEF{\cdot}5H_2O$; DEF = *N*,*N*-diethylformamide). The resultant nanoporous CeO_2 exhibited hierachically nanoporous structure and a crystalline framework, similar to *np*-MgO-500, and its N_2 adsorption isotherm indicated the coexistence of the micro- and mesopores, with a surface area of 100 m^2/g (see Figure S3).

It is noteworthy that thermal treatments converted the Mg-*aph*-MOF into 3D nanoporous MgO frameworks instead of discrete MgO nanoparticles embedded in a carbon matrix. We monitored the structural evolution of the Mg-*aph*-MOF with TEM images taken at each step of temperature increment (Figure 3a−f). As shown in Figure 3a and b, the crystals of Mg-*aph*-MOF did not show any changes until 160 °C, whereupon only noncoordinating guest molecules were lost. Upon heating up to 275 °C, irregular pores started to form (Figure 3c), primarily due to the evaporation of coordinating molecules (DMA and water). The pores might have been formed by the confinement of liberated coordinating guest molecules and organic ligands. These phenomena were also supported by the variable temperature XRPD patterns (see Figures S4 and S5). The XRPD pattern of as-synthesized Mg-*aph*-MOF showed strong reflections in the region 5−25°, which were commensurate with the simulated pattern from single crystal X-ray diffraction data (see Figure S4). Up to 160 °C the typical patterns of Mg-*aph*-MOF were retained, except for a slight broadening and shift of the peaks. However, above 275 °C all peaks from the crystalline Mg-*aph*-MOF disappeared, indicating that the MOF solid lost crystallinity as well as long-range orderings. When the temperature reached 350 °C, the pores were widely distributed over the solid, which implied the generation and confinement of large amounts of organic substances at the high temperature (Figure 3d). The shapes of the pores were still irregular, and the crystalline metal oxide had not yet formed. However, upon further heating to 500 °C, the size distribution of the spherical pores became narrower (Figure 3e), and the resultant solid started to show crystallinity (see Figure S5). Finally, after thermal treatment of Mg-*aph*-MOF at 500 °C for 12 h under inert atmosphere, highly crystalline 3D nanoporous MgO, *np*-MgO-500 was produced (Figure 3f). Comparison of the scanning electron microscopy (SEM) images and energy-dispersive X-ray spectroscopy (EDS) results for the cross sections of Mg-*aph*-MOF heated at 350 °C and *np*-MgO-500 also supported this evolution process; the former still possessed the organic porogens in the solid, but the latter contained a high distribution of pores and hierarchical structures (Figure 3g−i). To investigate the organic substances which were generated by thermolysis over each temperature range, the Mg-*aph*-MOF was analyzed by pyrolysis gas chromatography/mass spectrometry (py-GC/MS, Figure S6). As shown in Table S1, even below 300 °C, the evolution of new organic species was detected, and at higher temperature, many organic substances with high boiling points were generated. This indicated that during the thermal treatment of Mg-*aph*-MOF, decomposed organic fragments reacted to yield new species, which were confined in the solid until the temperatures were high enough to evaporate them.

Based on the above results, we suggest that organic substances generated during the thermal decomposition of the MOF formed vesicles, which acted as self-templates, and afterward were converted to nanopores. Meanwhile, inorganic SBUs nucleated and grew to nanocrystals at high temperature, but their growth was restricted to sizes below 10 nm due to the presence of the organic templates. Under subsequent high-temperature treatment, the organic vesicles were liberated, generating numerous spherical nanopores and a nanocrystalline metal oxide framework. There has, to the our best knowledge, been no reports of the successful preparation of 3D porous structures composed of metal oxides by the thermal decomposition of MOFs. We suggest that the high thermal and chemical stabilities of conventional aromatic organic ligands, which have been used in the majority of the previous work,[22−35] induce their preferential conversion into carbogenic structures, with the simultaneous agglomeration of the metal oxides. Therefore, MOFs composed of aromatic carboxylate ligands (*ar*-MOF) appear to be unsuitable precursors for the preparation of porous metal oxides. To test this hypothesis, we synthesized an aromatic ligand-based MOF (Mg-*ar*-MOF), $Mg_3(bpdc)_3(DMA)_4$ (bpdc = biphenyl-4,4′-dicarboxylate)

dx.doi.org/10.1021/ja401869h | J. Am. Chem. Soc. 2013, 135, 8940−8946

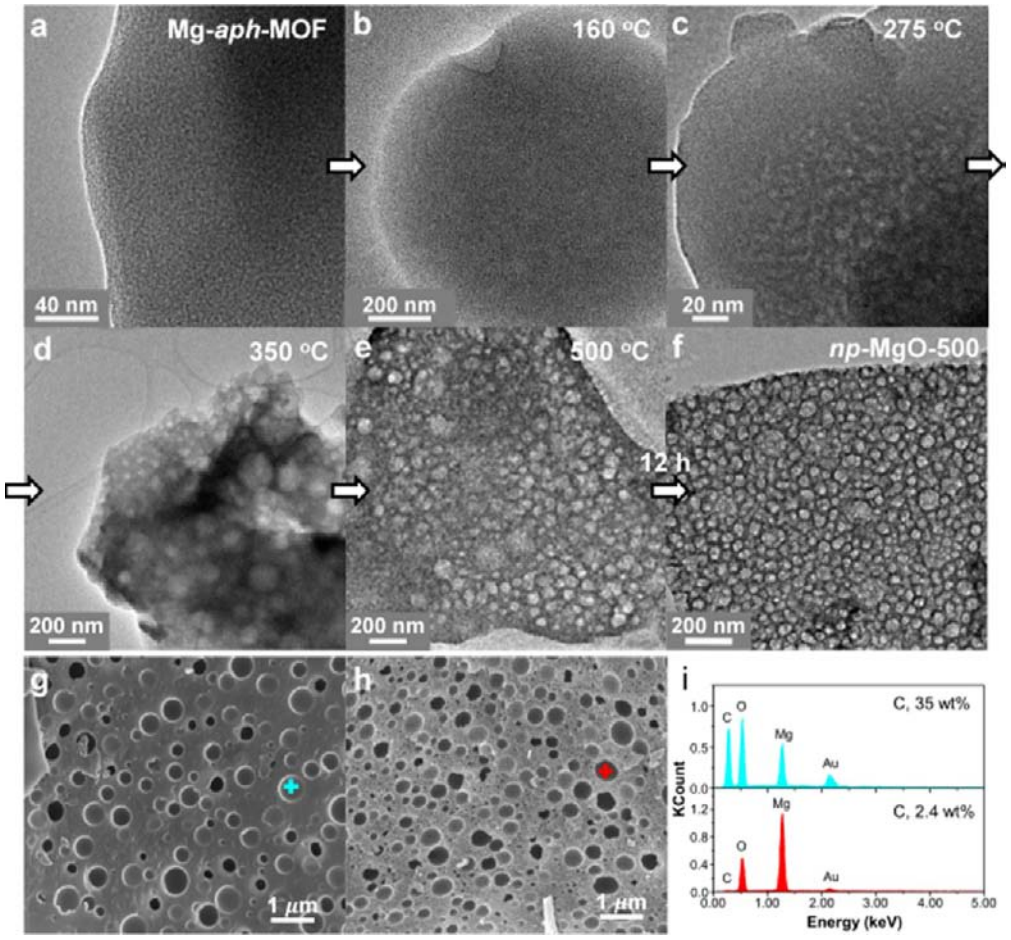

Figure 3. Temperature-dependent evolution of porous structures during conversion of Mg-*aph*-MOF to nanoporous MgO. HR-TEM images for Mg-*aph*-MOF (a) before and after heat treatment at (b)160 °C , (c) 275 °C, (d) 350 °C, and (e) 500 °C. (f) *np*-MgO-500. SEM images for (g) Mg-*aph*-MOF after heat treatment at 350 °C and (h) *np*-MgO-500. (i) EDS data for the positions, which are indicated with cross marks (green +, red +) in (g) and (h).

according to a previous report.[36] The thermolysis of the Mg-*ar*-MOF provided only aggregated MgO nanoparticles (Figure S7 and experimental details in the Supporting Information). Py-GC/MS results for Mg-*ar*-MOF revealed that new organic species were not formed, even at 450 °C, which means that there were no porogens to direct nanoporous structure formation during the decompostion and oxidiation of the MOF (Table S2 and Figure S8).

The contrasting results from the thermolysis of Mg-*aph*-MOF and Mg-*ar*-MOF highlight the competition between the duration of the organic vesicles and the evolution of the MgO nanoporous structure. The removal of organic vesicles that is faster than the structuring of the 3D porous structure may result in the agglomeration of MgO particles. The rapid conversion of Mg^{2+} incorporated in the MOF to MgO NCs would generate large MgO particles before forming the organic vesicles. This expectation was proven by the thermal treatment of Mg-*aph*-MOF under oxygen atmosphere instead of nitrogen gas flow. As shown in Figure S9, the product was composed of highly crystalline cubic-shaped MgO nanocrystals of ~50 nm in size. In addition, we carried out a control expreriment to confirm the role of extended structure in the MOF for the successful generation of nanoporous structure. For this purpose, a small coordination molecule composed of Mg^{2+} and pentanoate ($Mg(CH_3(CH_2)_3COO)_2$) was heated at 400 °C under nitrogen for 12 h. As shown in Figure S10, while the resulting solid was single-phase cubic MgO NC (~10 nm), those particles constructed a random agglomeration instead of the nanoporous structure.

Based on our understanding of the formation mechanism of the Mg-*aph*-MOF, we speculate that the thermal conversion conditions, such as gas flow and temperature ramping rates, can be critical factors for determining the size of the organic vesicles, which consequently control the nanopore size. For instance, when Mg-*aph*-MOF was thermally treated with a 10-fold faster ramping rate (50 °C/min), nanoporous MgO with a much smaller pore size (~20 nm) (*np*-MgO-500-fast T, Figure 4a) than that of *np*-MgO-500 (50−100 nm) (Figure 4b) was obtained, which was due to the fast transport and removal of organic vesicles before they could congregate. In contrast, thermal treatment of Mg-*aph*-MOF under static nitrogen atmosphere without flow would promote the growth of the organic vesicles, thus resulting in larger pores, around 100 nm (*np*-MgO-500-no flow, Figure 4c). Under such a condition, the evaporation of organic vesicles to generate nanopores would be suppressed, compared to the condition where nitrogen was flowed. Consequently, the organic vesicles contained in the structure can migrate together to form enlarged organic moieties, which afterward converted into larger pores. Nitrogen adsorption isotherm results also supported the synthesis of pore size-controlled MgO nanostructures (Figure 4d−f). Since the rapid escape of small organic vesicles in MgO synthesized with

dx.doi.org/10.1021/ja401869h | *J. Am. Chem. Soc.* 2013, 135, 8940−8946

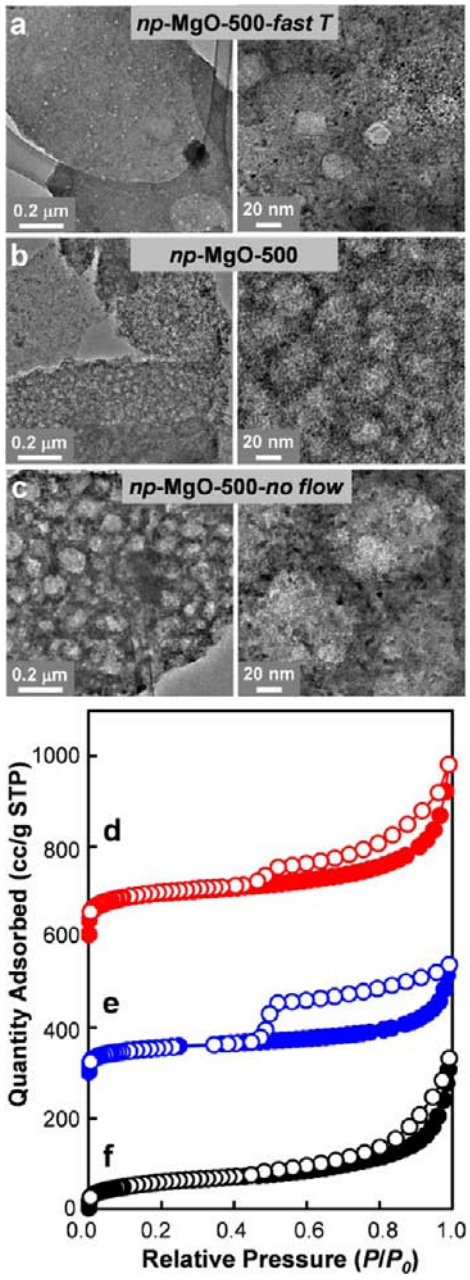

Figure 4. Pore size control of *np*-MgO under different reaction conditions. TEM images and N_2 sorption isotherms for (a,d) *np*-MgO-500-fast T , (b,e) *np*-MgO-500, and (c,f) *np*-MgO-500-no flow, respectively. For clarity, N_2 sorption isotherms were shifted upward by 300 and 600 cc/g, respectively.

rapid heating rates (Figure 4a) generated a high proportion of the micropores, the N_2 adsorption showed a large uptake at pressures below 0.01 atm, and the pore volume for the micropores reached 0.20 cc/g out of a total pore volume of 0.59 cc/g.

To explore the advantages of the hierarchically nanoporous MgO with a nanocrystalline framework, we studied the behavior of *np*-MgO as a carbon dioxide gas adsorbent. Chemisorbents for CO_2 removal are mostly based on alkaline earth metal oxides, such as MgO and CaO, wherein abundant basic sites are capable of strongly interacting with the acidic nature of CO_2.[37,38] However, high regeneration temperature and poor recyclability of such metal oxides during CO_2 adsorption−desorption process commonly impede their widespread use. We hypothesized that our *np*-MgO with hierarchical nanoporosity and structural robustness would be well suited for CO_2 adsorbent with high capacity and recyclability. The CO_2 gas cycling experiments were conducted using a TGA apparatus with a flow of 15% (v/v) CO_2 in N_2, which mimicked flue gas. As-prepared *np*-MgO-500 absorbed 5.2 wt % CO_2 at 27 °C (Figure 5a). After eight cycles of CO_2 adsorption/desorption over *np*-MgO-500, TEM images showed that the nanocrystalline framework became aggregated, generating secondary nanoparticles. Also, the nanopores (~100 nm) in the as-prepared *np*-MgO-500 were reduced to around 20 nm in size (Figure 5b). The small carbon content (1.76 wt %) in *np*-MgO-500 was inadequate to sustain the hierarchically nanoporous MgO structure during the several cycles of adsorption/desorption, because *np*-MgO-500 suffers from significant changes in the crystal systems between MgO (cubic) and $MgCO_3$ (trigonal). To increase the carbon content as an adhesive and protectant, but to still provide the hierarchical structure, the thermal treatment of Mg-*aph*-MOF was conducted at a lower temperature, 350 °C, for 12 h under inert atmosphere. The resultant solid, designated as *np*-MgO-350, was a nanoporous, dark-brown solid with a carbon content of 10 wt %. The BET surface area was 160 m^2/g (see Figure S11). As shown in Figure 5c, the CO_2 uptake capacity of *np*-MgO-350 at 27 °C was much higher than *np*-MgO-500 at 9.2 wt %, which was the highest recorded value for MgO nanomaterials under similar conditions[39−41] and was 12 times better than commercially available 50 nm-sized MgO powder (0.76 wt %) (Tables S3 and S4 and Figure S12). This capacity is also comparable with the result from the Mg-based MOF, Mg_2(dobpdc) (dobpdc^{4-} = 4,4′-dioxido-3,3′-biphenyldicarboxylate), which showed 2.52 mmol/g and 9.9 wt % upon exposure to flowing 15% CO_2 in N_2 at 40 °C.[42] More importantly, even after eight cycles of CO_2 adsorption/desorption, the hierarchically nanoporous structures of *np*-MgO-350 remained intact, as evidenced by TEM (Figure 5d). Since acidic CO_2 molecules are adsorbed at low-coordinated and basic O^{2-}−Mg^{2+} sites on MgO, a high surface area which provides many edge- and corner-located oxygen atoms is critical to the CO_2 capacity of MgO adsorbents.[37,38] Therefore, in the present work, hierarchically porous MgO prepared by our MOF-driven method assured superior performance associated with facile mass transport and recyclability. In addition, the large population of surface defect sites on the MgO nanocrystals comprising the framework wall may allow for a low regeneration temperature of 300 °C (Figure S13), which affords a definite advantage for practical application.

3. CONCLUSIONS

In conclusion, we have developed a novel, simple method to synthesize hierarchically nanoporous frameworks of nanocrystalline metal oxides, such as magnesia and ceria, by the thermal conversion of well-designed MOFs. The introduction of aliphatic ligands to MOFs as an organic building block was the key to controlling the thermal stability and inducing the self-templating effect. By controlling the thermolysis conditions, such as temperature, rate of temperature increase, and carrier gas flow rate, we could readily engineer the pore sizes of MgO as well as the carbon support content. In addition, because of the high surface area and hierarchically porous structure of the nanoporous MgO, it performed exceptionally in the uptake of CO_2 gas under mimicked flue gas conditions. Therefore, this

dx.doi.org/10.1021/ja401869h | J. Am. Chem. Soc. 2013, 135, 8940−8946

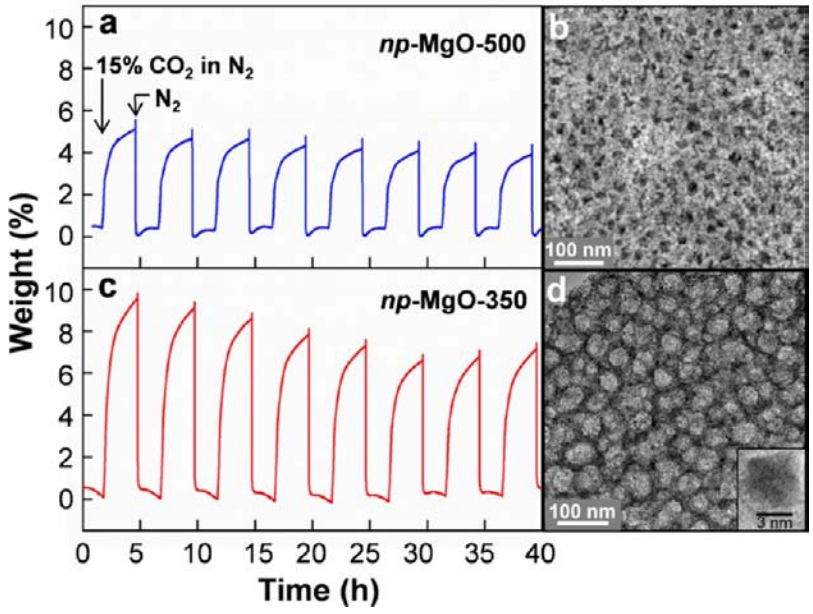

Figure 5. Studies of *np*-MgO upon carbon dioxide gas cycling experiment. (a,c) Gas cycling result and (b,d) TEM image after the cycles for *np*-MgO-500 and *np*-MgO-350, respectively.

approach to aliphatic ligand-based MOF decomposition can be expanded to other nanoporous monometallic and multimetallic oxides with a multitude of potential applications, especially for energy-related materials.

4. MATERIALS AND METHODS

All chemicals and solvents were of reagent grade and used without further purification. Infrared spectra were recorded with a Thermo-Fisher Scientific iS10 FT-IR spectrometer. Elemental analyses were performed at the UNIST Central Research Facilities (UCRF) in Ulsan National Institute of Science and Technology (UNIST). TGA was performed under N_2(g) at a scan rate of 5 °C min^{-1}, using a TGA Q50 from TA Instruments. XPS was performed on a K-alpha from Thermo Fisher. The chemical composition of MgO was analyzed by inductively coupled plasma-mass spectrometry (ICP-MS, PerkinElmer, ELAN DRC-e). XRPD data were recorded on a Bruker D8 advance diffractometer at 40 kV and 40 mA for Cu Kα (λ = 1.54050 Å), with a step size of 0.02° in 2θ. HR-TEM images and EDS were obtained on a JEOL JEM-2100 microscope.

Preparation of Mg-*aph*-MOF ({[Mg_4(adipate)$_4$(DMA)-(H_2O)]·5DMA·2MeOH·4H_2O}). Adipic acid (0.053 g, 0.36 mmol) was dissolved in DMA (4 mL) and mixed with an MeOH (2 mL) solution of $Mg(NO_3)_2$·6H_2O (0.084 g, 0.33 mmol). The solution was heated in a Teflon vessel in an autoclave at 120 °C for 24 h and then cooled to room temperature. Colorless rod-shaped crystals formed, which were filtered, and washed briefly with the mother liquor. Yield: 44 mg (38%). Anal. calcd for $Mg_4C_{50}H_{104}N_6O_{29}$: C, 44.46; H, 7.76; N, 6.22. Found: C, 44.45; H, 7.03; N, 6.17. FT-IR (Nujol mull): ν_{OH}, 3374 (m, br); $\nu_{C=O}$, 1651 (br); $\nu_{O-C=O}$, 1605, 1560 (s) cm^{-1}.

Preparation of *np*-MgO-350 and *np*-MgO-500. Solid Mg-*aph*-MOF was ground into a powder and then heated at 5 °C/min under a nitrogen flow of 60 mL/min. After reaching the target temperature (350 and 500 °C, respectively), the material was maintained at the temperature for 12 h and then cooled to room temperature. The resultant solid, *np*-MgO-350, was dark-brown, whereas *np*-MgO-500 was obtained as a white powder.

Preparation of Ce-*aph*-MOF ({Ce_2(adipate)$_3$·2DEF·5H_2O}). Adipic acid (0.022 g, 0.15 mmol) was dissolved in *N*,*N*-diethylformamide (DEF, 2.5 mL) and mixed with a DEF (2.5 mL) solution of $Ce(NO_3)_3$·6H_2O (0.044 g, 0.10 mmol). The solution was sealed in a glass jar, heated at 110 °C for 24 h, and then cooled to room temperature. Pale-yellow needle-shaped crystals formed, which were filtered and washed briefly with the mother liquor. Yield: 22 mg (44%). Anal. calcd for $Ce_2C_{48}H_{96}O_{21}N_6$: C, 41.97; H, 7.04; N, 6.12. Found: C, 42.10; H, 6.88; N, 6.07. FT-IR (Nujol mull): ν_{OH}, 3444 (m, br); $\nu_{C=O}$(noncoordinating DEF), 1680 (s); $\nu_{C=O}$(coordinating DEF), 1650 (s); $\nu_{O-C=O}$, 1570 (s) cm^{-1}.

Preparation of *np*-CeO_2. Solid Ce-*aph*-MOF was ground into a powder and then heated at 5 °C/min under a nitrogen flow of 60 mL/min. After reaching the target temperature of 500 °C, the material was maintained at that temperature for 12 h and then cooled to room temperature. The resultant black solid was ground into a powder. The powder was heated 1 °C/min to 300 °C under an oxygen flow of 100 mL/min. After the material was maintained at this temperature for 2 h and then cooled to room temperature, pale-yellow *np*-CeO_2 was obtained.

Preparation of *ar*-MgO. Mg_3(bpdc)$_3$(DMA)$_4$ (Mg-*ar*-MOF) was heated at 5 °C/min to 600 °C under a nitrogen flow of 60 mL/min. The material was maintained at this temperature for 12 h and then cooled to room temperature.

Gas Sorption Study. The nitrogen adsorption−desorption isotherms were measured at 77 K on a BELsorp-MAX adsorption analyzer. Prior to adsorption measurement, the samples were evacuated at 200 °C under vacuum ($p < 10^{-5}$ mbar) for 12 h. The specific surface area was determined from the linear part of the BET equation, and the total pore volume was calculated from the amount adsorbed at a relative pressure of about 0.99. The results were summarized in Table S5.

Single-Crystal X-ray Crystallography. A single-crystal of Mg-*aph*-MOF was mounted on the top of a capillary with Paratone oil. Diffraction data were collected at 173 K using a Rigaku R-axis Rapid II diffractometer (Mo Kα, λ = 0.71073 Å), which was equipped with an XRD camera system with an imaging plate. Full sphere data were collected for all the crystals, and the raw data were processed and scaled using the RapidAuto software suite.[43] The crystal structures were solved by direct methods[44] and refined by full-matrix least-squares refinement using the SHELXL-97 computer program.[45] The positions of all nonhydrogen atoms were refined with anisotropic displacement factors. The hydrogen atoms were positioned geometrically using a riding model. For Mg-*aph*-MOF, the electron density of the disordered guest molecules was flattened using the 'SQUEEZE' option of the program PLATON.[46] The crystallographic data and selected bond lengths and angles of Mg-*aph*-MOF are summarized in Tables S6 and S7.

dx.doi.org/10.1021/ja401869h | *J. Am. Chem. Soc.* 2013, 135, 8940−8946

■ ASSOCIATED CONTENT

Supporting Information

Crystallographic data as a CIF file, Table S1−7, Figures S1−13, and related references. This material is available free of charge via the Internet at http://pubs.acs.org.

■ AUTHOR INFORMATION

Corresponding Author

hoirimoon@unist.ac.kr; shjoo@unist.ac.kr

Author Contributions

[§]These authors contributed equally.

Notes

The authors declare no competing financial interest.

■ ACKNOWLEDGMENTS

This work was supported by the Basic Science Research Program through the National Research Foundation of Korea (NRF) funded by the Ministry of Education, Science and Technology (NRF-2010-0009063 and NRF-2010-0005341), the Ministry of Knowledge Economy (MKE), Korea Institute for Advancement of Technology (KIAT) through the Inter-ER Cooperation Projects. S.H.J. acknowledges T. J. Park Junior Faculty Fellowship supported by the T. J. Park Foundation.

■ REFERENCES

(1) Davis, M. E. *Nature* **2002**, *417*, 813.
(2) Kresge, C. T.; Leonowicz, M. E.; Roth, W. J.; Vartuli, J. C.; Beck, J. S. *Nature* **1992**, *359*, 710.
(3) Corma, A. *Chem. Rev.* **1997**, *97*, 2373.
(4) Wan, Y.; Zhao, D. *Chem. Rev.* **2008**, *107*, 2821.
(5) Schüth, F. *Chem. Mater.* **2001**, *13*, 3184.
(6) Ren, Y.; Ma, Z.; Bruce, P. G. *Chem. Soc. Rev.* **2012**, *41*, 4909.
(7) Lee, J.; Orilall, M. C.; Warren, S. C.; Kamperman, M.; DiSalvo, F. J.; Wiesner, U. *Nat. Mater.* **2008**, *7*, 222.
(8) Yang, P.; Zhao, D.; Margolese, D. I.; Chmelka, B. F.; Stucky, G. D. *Nature* **1998**, *396*, 152.
(9) Grosso, D.; Boissière, C.; Smarsly, B.; Brezesinski, T.; Pinna, N.; Albouy, P. A.; Amenitsch, H.; Antonietti, M.; Sanchez, C. *Nat. Mater.* **2004**, *3*, 787.
(10) Yang, H.; Zhao, D. *J. Mater. Chem.* **2005**, *15*, 1217.
(11) Corma, A.; Atienzar, P.; Garcia, H.; Chane-Ching, J.-Y. *Nat. Mater.* **2004**, *3*, 394.
(12) Buonsanti, R.; Pick, T. E.; Krins, N.; Richardson, T. J.; Helms, B. A.; Milliron, D. J. *Nano Lett.* **2012**, *12*, 3872.
(13) Kondo, J. N.; Domen, K. *Chem. Mater.* **2008**, *20*, 835.
(14) Yaghi, O. M.; O'Keeffe, M.; Ockwig, N. W.; Chae, H. K.; Eddaoudi, M.; Kim, J. *Nature* **2003**, *423*, 705.
(15) Tranchemontagne, D. J.; Mendoza-Cortes, J. L.; O'Keeffe, M.; Yaghi, O. M. *Chem. Soc. Rev.* **2009**, *38*, 1257.
(16) Murray, L. J.; Dincă, M.; Long, J. R. *Chem. Soc. Rev.* **2009**, *38*, 1294.
(17) Makal, T. A.; Li, J.-R.; Lu, W.; Zhou, H. -C. *Chem. Soc. Rev.* **2012**, *41*, 7761.
(18) Corma, A.; Garcia, H.; Xamena, F. X. L. I. *Chem. Rev.* **2010**, *110*, 4606.
(19) Bureekaew, S.; Sato, H.; Matsuda, R.; Kubota, Y.; Hirose, R.; Kim, J.; Kato, K.; Takata, M.; Kitagawa, S. *Angew. Chem., Int. Ed.* **2010**, *49*, 7660.
(20) Pramanik, S.; Zheng, C.; Zhang, X.; Emge, T. J.; Li, J. *J. Am. Chem. Soc.* **2011**, *133*, 4153.
(21) Rocca, J. D.; Liu, D.; Lin, W. *Acc. Chem. Res.* **2011**, *44*, 957.
(22) Yang, S. J.; Park, C. R. *Adv. Mater.* **2012**, *24*, 4010.
(23) Yang, S. J.; Kim, T.; Im, J. H.; Kim, Y. S.; Lee, K.; Jung, H.; Park, C. R. *Chem. Mater.* **2012**, *24*, 464.
(24) Hu, J.; Wang, H.; Gao, Q.; Guo, H. *Carbon* **2010**, *48*, 3599.
(25) Chaikittisilp, W.; Hu, M.; Wang, H.; Huang, H.-S.; Fujita, T.; Wu, K. C.-W.; Chen, L. -C.; Yamauchi, Y.; Ariga, K. *Chem. Commun.* **2012**, *48*, 7259.
(26) Lim, S.; Suh, K.; Kim, Y.; Yoon, M.; Park, H.; Dybtsev, D. N.; Kim, K. *Chem. Commun.* **2012**, *48*, 7447.
(27) Jiang, H.-L.; Liu, B.; Lan, Y. -Q.; Kuratani, K.; Akita, T.; Shioyama, H.; Zong, F.; Xu, Q. *J. Am. Chem. Soc.* **2011**, *133*, 11854.
(28) Parast, M. S. Y.; Morsali, A. *Inorg. Chem. Commun.* **2011**, *14*, 645.
(29) Liu, B.; Zhang, X.; Shioyama, H.; Mukai, T.; Sakai, T.; Xu, Q. *J. Power Sources* **2010**, *195*, 857.
(30) Wang, W.; Li, Y.; Zhang, R.; He, D.; Liu, H.; Liao, S. *Catal. Commun.* **2011**, *12*, 875.
(31) Cho, W.; Park, S.; Oh, M. *Chem. Commun.* **2011**, *47*, 4138.
(32) Das, R.; Pachfule, P.; Banergee, R.; Poddar, P. *Nanoscale* **2012**, *4*, 591.
(33) Xu, X.; Cao, R.; Jeong, S.; Cho, J. *Nano Lett.* **2012**, *12*, 4988.
(34) Ma, S.; Goenaga, G. A.; Call, A. V.; Liu, D.-J. *Chem.—Eur. J.* **2011**, *17*, 2063.
(35) Masoomi, M. Y.; Morsali, A. *Coor. Chem. Rev.* **2012**, *256*, 2921.
(36) Davies, R. P.; Less, R. J.; Lickiss, P. D.; White, J. P. *Dalton Trans.* **2007**, 2528.
(37) Meis, N.; Bitter, J. H.; de Jong, K. P. *Ind. Eng. Chem. Res.* **2010**, *49*, 1229.
(38) Daub, C. D.; Patey, G. N.; Jack, D. B.; Sallabi, A. K. *J. Chem. Phys.* **2006**, *124*, 114706.
(39) Ruminski, A. M.; Jeon, K.-J.; Urban, J. J. *J. Mater. Chem.* **2011**, *21*, 11486.
(40) Bhagiyalakshmi, M.; Lee, J. Y.; Jang, H. T. *Int. J. Greenhouse Gas Control* **2010**, *4*, 51.
(41) Gregg, S. J.; Ramsay, J. D. *J. Chem. Soc. A* **1970**, 2784.
(42) McDonald, T. M.; Lee, W. R.; Mason, J. A.; Wiers, B. M.; Hong, C. S.; Long, J. R. *J. Am. Chem. Soc.* **2012**, *134*, 7056.
(43) *RapidAuto software*, R-Axis series, Cat. No. 9220B101; Rigaku Corporation: The Woodlands, TX, 1998.
(44) Sheldrick, G. M. *Acta Crystallogr.* **1990**, *A46*, 467.
(45) Sheldrick, G. M. *SHELXL97, Program for the crystal structure refinement*; University of Göettingen: Göettingen, Germany, 1997.
(46) Sluis, P.; Speck, A. L. *Acta Crystallogr., Sect. A* **1990**, *46*, 194.